JOURNAL OF CATALYSIS 153, 317–332 (1995)

Total Oxidation of Carbon Monoxide and Methane over Transition Metal–Fluorite Oxide Composite Catalysts

II. Catalyst Characterization and Reaction Kinetics

Wei Liu and Maria Flytzani-Stephanopoulos*,[1]

Department of Chemical Engineering, Massachusetts Institute of Technology, Cambridge, Massachusetts 02139; and
**Department of Chemical Engineering, Tufts University, Medford, Massachusetts 02155*

Received August 2, 1994; revised January 9, 1995

Cu–Ce–O and Au–Ce–O catalysts were characterized by XRD, XPS, and STEM. Copper in small amounts showed a strong tendency to associate with cerium oxide. When the cerium oxide surface was saturated with copper, excess copper formed bulk copper oxide particles. The cuprous (+1) oxidation state was identified by XPS for the copper clusters distributed in cerium oxide, while gold in the Au–Ce–O catalyst was in the form of metallic particles distributed in the cerium oxide matrix. The reaction kinetics of CO and methane oxidation over the Cu–Ce–O catalysts were measured at a partial pressure of CO or oxygen from 0.001 to 0.06 bar, at a partial pressure of methane from 0.001 to 0.03 bar, and at temperatures ranging from 40 to 200°C for CO oxidation and from 400 to 550°C for methane oxidation. The oxidation rates of CO and methane over the Cu–Ce–O catalysts were expressed as $kK_RP_RP_O''/(1 + K_RP_R)$, where P_R denotes the partial pressure of CO or methane and P_O is the partial pressure of oxygen. CO oxidation kinetics over the Au–Ce–O catalyst were described by $kP_{CO}^{0.3}P_O^{0.18}$. The kinetic results were interpreted with the Langmuir–Hinshelwood mechanism and in terms of a synergistic effect resulting from the interaction of the two kinds of materials. © 1995 Academic Press, Inc.

1. INTRODUCTION

Transition metal–fluorite oxide composite catalysts were evaluated in the preceding paper for the total oxidation of CO and methane (1). The Cu–Ce–O system was identified as one of the most active catalyst systems. The significant enhancement of catalytic activity and resistance to water vapor for CO oxidation observed with this catalyst cannot be explained on the basis of copper dispersion alone. Thus, a strong interaction between these two kinds of materials was proposed. Strong interaction between a metal particle and its oxide support has long been a fascinating catalysis subject (2–7). Moreover, another concept involving new active sites created at the interface between metal and support has been proposed (6, 7).

Although a mechanistic understanding of the correlation between catalyst properties and metal–support interactions is still limited, looking at the oxide support not simply as an inert carrier has given many insights into new catalyst development. For example, Frost (8) predicted the existence and properties of new methanol synthesis catalysts by using the minute Schottky junction theory at the interface between metals and oxides. In studies of CO hydrogenation, the strong precious metals–TiO_2 interaction has been considered a classic system in this field. The strong interaction between precious metals and cerium oxide has been another active area (9) in environmental catalysis because of the widespread use of cerium oxide in the precious metal-based automotive catalytic converter. The enhanced CO oxidation activity and stability of precious metal catalysts by yttria-stabilized zirconia (YSZ) support were recently reported and explained in terms of interfacial reactions (10). A reaction mechanism based on the metal–support interface was also proposed for some low temperature CO oxidation catlaysts, such as Pt/SnO_2 (11), Pd/SnO_2 (12, 13), Au/α-Fe_2O_3, or TiO_2 (14). In a recent study of a nonprecious metal–fluorite oxide system for CO oxidation, a geometric interfacial interaction in Cu/YSZ involving surface oxygen vacancy was proposed (15).

In this work we characterized the Au–Ce–O and Cu–Ce–O catalyst systems by X-ray photoelectron spectroscopy (XPS) and scanning transmission electron microscopy (STEM) aided by X-ray microprobe analysis, and measured the reaction kinetics in order to elucidate the strong interaction between copper and cerium oxide and its effect on catalytic activity. The Au–Ce–O catalyst

[1] To whom correspondence should be addressed.

0021-9517/95 $6.00

clearly demonstrated a synergistic effect on catalytic activity and best served as a reference.

2. EXPERIMENTAL

2.1. Catalyst Preparation and Characterization

Bulk composite catalysts were prepared by coprecipitating the aqueous salt solutions of the metals with ammonium carbonate or sodium carbonate. The CeO_2 support was prepared by thermal decomposition of cerium acetate hydrate (99.9%, Aldrich). The supported catalysts were prepared by conventional wet impregnation using the aqueous salt solution of the metal. The mixture of cerium oxide and copper oxide was prepared by mixing the CuO and CeO_2 powder with water and drying it for 1 h at 300°C. The details of the preparation procedure were described in the preceding paper (1). The cerium precursor used for coprecipitation was low purity (99%) cerium nitrate (from Aldrich) containing 1.5 wt% lanthanum. This type of cerium is designated Ce(La) in the catalyst formula throughout this paper. The catalyst characterization was performed by nitrogen adsorption/desorption on a Micromeritics ASAP 2000 apparatus for BET surface area and pore size measurement and by X-ray powder diffraction (XRD) on a Rigaku 300 X-ray diffractometer for crystalline identification. The catalyst typically had an average pore size of 20 nm and a BET surface area from 20 to 57 m^2/g. For the XRD analysis, copper $K\alpha_1$ radiation was used with a power setting of 50 kV and 200 mA. The divergence slit, scattering slit, and receiving slit were 1°, 1°, and 0.15°, respectively. The data were acquired at a 2θ interval of 0.02°. The catalyst microstructure analysis was performed on a state-of-the-art Vacuum Generators HB603 scanning transmission electron microscope equipped with an X-ray microprobe of 0.14 nm optimum resolution. For STEM analysis, the catalyst powder was dispersed on a nickel grid coated by a carbon film and the elemental maps were acquired on a 128 × 128 data matrix. The catalyst surface composition was determined by X-ray photoelectron spectroscopy with a Perkin–Elmer 5100 system. For XPS analysis, the catalyst powder was pressed on a tantalum foil and placed into the vacuum chamber without any pretreatment. A Mg electron source was used with a power setting of 15 kV and 300 W. The binding energy was adjusted to the C1*s* peak at 284.6 eV which existed in all measurements. The Auger kinetic energy was calculated by $1253.6 - (BE)_A$, where $(BE)_A$ is the measured binding energy of the Auger L_3VV line.

2.2. Apparatus and Procedure

The reactor was a 0.6 cm i.d. × 50 cm long quartz tube heated by a Lindberg furnace. The reaction temperature was monitored by a quartz glass-sheathed K-type thermocouple placed at the top of the packed catalyst bed. CO and CH_4 reacting gases were certified calibration gas mixtures balanced by helium (from Matheson). Air and helium (all from AIRCO) were used as oxidizing gas and diluent, respectively. The gas streams were measured with mass flow controllers and mixed prior to the reactor inlet. The resulting gas mixture without further purification flowed downward through the packed bed. For kinetic measurements, the reactor was operated in a differential mode with the conversion not exceeding 10% so that the temperature was nearly uniform in the packed catalyst bed. Separate experimental tests showed that bulk mass transfer and intraparticle mass transfer resistance could be eliminated by using a gas flow rate greater than 200 sccm and catalyst particles of less than 150 μm in size. Therefore, a total gas flow rate of 400 sccm and an average catalyst particle size of 100 μm were used for the kinetics study. The reaction conversion was controlled by the catalyst loading, while the catalyst was diluted by silicon carbide to about 10 mm packed height. The partial pressure of the reacting gas species was varied over the range of 0.001 to 0.09 bar. CO oxidation over the Au–Ce–O catalyst was measured over the temperature range of 10 to 50°C. CO oxidation and methane oxidation over the Cu–Ce–O catalysts were conducted at temperatures from 40 to 200°C and from 400 to 550°C, respectively. Before any kinetic measurement, the catalyst was always treated for 1 h in the reaction gas mixture at 300°C for CO oxidation and at 600°C for methane oxidation. Carbon dioxide concentration in the product gas stream was analyzed by a HP5880A gas chromatograph (GC) with a thermal conductivity detector (TCD). The production of CO_2 was used to calculate the reaction rate

$$\text{Rate} = N_t \cdot X_{CO_2}/W_{cat}, \qquad [1]$$

where N_t is the total molar gas flowrate in mols/s, X_{CO_2} is the molar fraction of CO_2 in the product gas stream, and W_{cat} is the catalyst weight in grams.

3. RESULTS

3.1. Catalyst Characterization

3.1.1. Characterization of $Au_{0.05}[Ce(La)]_{0.95}O_x$ catalyst. Only the 5 at.% Au-containing Au–Ce–O catalyst, $Au_{0.05}[Ce(La)]_{0.95}O_x$, was extensively characterized, because this catalyst showed better activity than the other Au–Ce–O catalysts of lower or higher gold content. Figures 1a–1c show the XRD pattern, STEM elemental maps, and XPS spectra for the $Au_{0.05}[Ce(La)]_{0.95}O_x$ catalyst. The XRD pattern in Fig. 1a consisted of CeO_2 and metallic gold crystal phases. The gold particle size calcu-

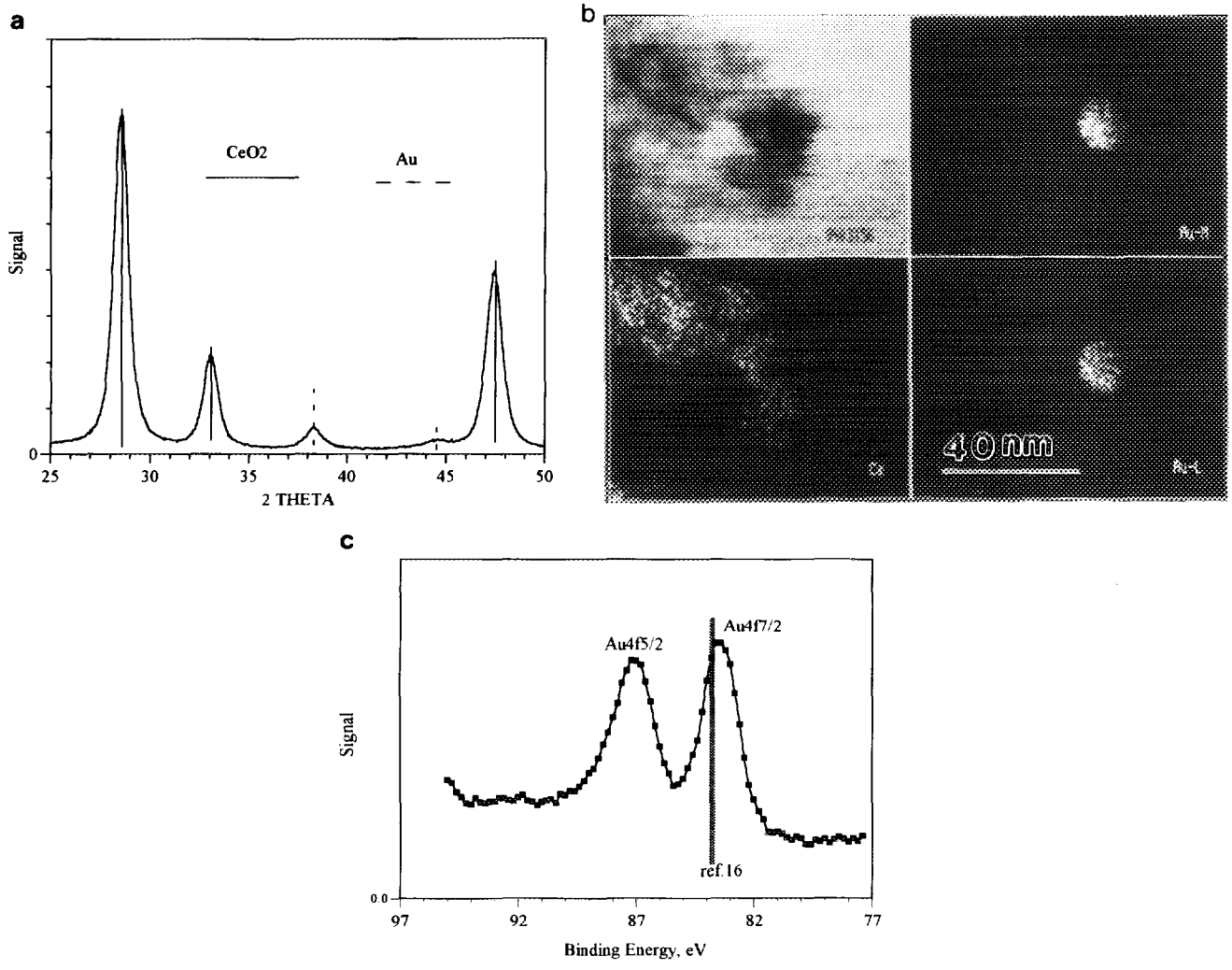

FIG. 1. (a) XRD pattern of the $Au_{0.05}[Ce(La)]_{0.95}O_x$ catalyst; (b) STEM/EDX elemental maps of the $Au_{0.05}[Ce(La)]_{0.95}O_x$ catalyst; (c) XP spectra of Au4*f* in the $Au_{0.05}[Ce(La)]_{0.95}O_x$ catalyst.

lated from the peak broadening is about 8 nm. The gold particles were difficult to visualize by electron microscopy because of the interference from cerium. However, clear images were obtained by elemental mapping with the STEM X-ray microprobe. STEM analysis indicated a uniform distribution of small gold particles in the cerium oxide matrix. The gold particle sizes varied from 1 nm to tens of nm. There was no evidence of epitaxial growth of the gold particles on cerium oxide or spillover of gold onto cerium oxide. The gold particle image in Fig. 1b shows that the well-rounded gold particle was in intimate contact with cerium oxide. The binding energy of $Au4f_{7/2}$ in the XPS was close to that of metallic gold given in the literature (16). These results indicate that in the $Au_{0.05}[Ce(La)]_{0.95}O_x$ catalyst small metallic gold particles of an average size of 8 nm were evenly distributed in the cerium oxide matrix and were in intimate contact with the cerium oxide.

3.1.2. XRD and STEM analyses of Cu–Ce–O catalyst system. A few XRD analyses of the Cu–Ce–O catalysts prepared by coprecipitation were reported in the preceding paper (1). For compositions of up to 15 at.% copper content, no CuO peaks were found by XRD. Figure 2 shows the XRD pattern of Cu–Ce–O catalysts containing 15 at.% or higher copper prepared by coprecipitation, impregnation, and physical mixing methods. The major peaks were due to the CeO_2 crystal phase. CuO appeared in smaller peaks and increased with copper content. No Cu_2O phase was found by XRD. Among three Cu–Ce–O catalysts containing 15 at.% Cu, the coprecipitated catalyst showed the lowest CuO phase intensity and the mixed oxide showed the highest CuO phase. We tried to correlate the variation of CeO_2 lattice spacing with copper content and catalyst preparation, but the results were inconclusive. Overall, limited information was obtained from the XRD study.

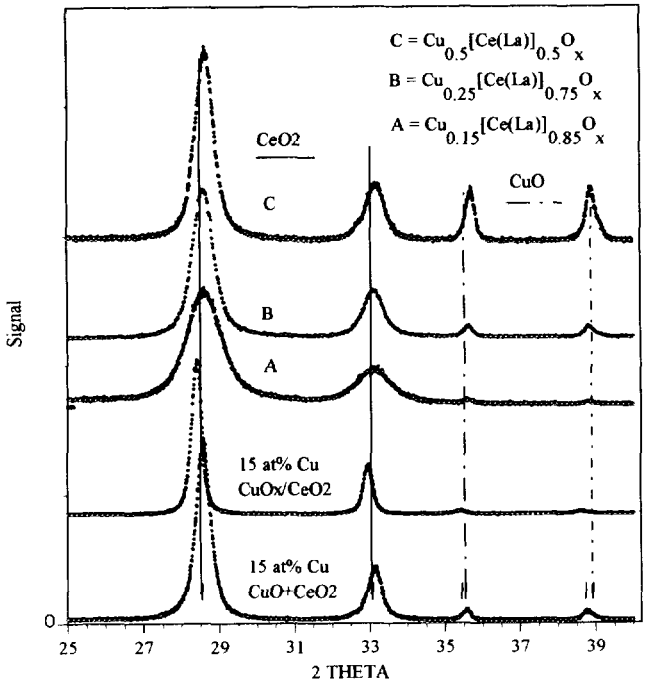

FIG. 2. XRD patterns of various Cu–Ce–O catalysts (wet mixture of CuO + CeO_2 was dried for 1 h at 300°C and all the others were prepared by 4-h calcination at 650°C in air).

The microstructure of the Cu–Ce–O system was first analyzed by high resolution transmission electron microscopy (HRTEM). Unlike alumina-supported precious metals, copper in the Cu–Ce–O catalyst could not be distinguished from cerium under electron microscopy because it is lighter than cerium. STEM, having both high magnification and elemental analysis functions, was found to be effective for the Cu–Ce–O catalyst characterization. The Cu–Ce–O catalyst was extensively analyzed by STEM. A few typical elemental maps are presented in Fig. 3. Figure 3a shows an elemental map of the coprecipitated $Cu_{0.15}[Ce(La)]_{0.85}O_x$ catalyst, illustrating an extensive dispersion of copper in the cerium oxide matrix. We assign the small copper spots (a few nm) in Fig. 3a to copper clusters, in view of the immiscibility of copper oxide and cerium oxide, while the big copper spots (>10 nm) are apparently bulk CuO particles. Figures 3b and 3c show the elemental maps of the impregnated catalyst, 15 at.% CuO_x/CeO_2, and the physical mixture 15 at.% CuO + CeO_2, respectively. Impregnation did not result in a uniform deposition of copper on cerium oxide. But, the physical mixing generated not only a mechanical mixture but also spillover of copper onto the cerium oxide. In the CuO + CeO_2 catalyst, a number of bulk copper oxide particles were found, but copper clusters also existed in the cerium oxide matrix. Qualitatively, a higher number of bulk copper oxide particles were found with the CuO_x/CeO_2 and CuO + CeO_2 catalysts than the $Cu_{0.15}[Ce(La)]_{0.85}O_x$. In contrast, more clusters were observed with the $Cu_{0.15}[Ce(La)]_{0.85}O_x$ than the other two 15 at.% copper-containing catalysts. These results are consistent with the smaller CuO peaks in the XRD pattern of the $Cu_{0.15}[Ce(La)]_{0.85}O_x$. In the preceding paper we reported that only bulk CuO in the Cu–Ce–O system could be removed by nitric acid. This conclusion is evidenced by the elemental map in Fig. 3d for the $Cu_{0.15}[Ce(La)]_{0.85}O_x$ catalyst after it was immersed in nitric acid for 14 h, filtered, and washed with deionized water. Very few bulk CuO particles remained in this nitric-acid-treated catalyst, compared to the fresh one. However, the copper clusters remained intact.

Figure 3e shows an elemental map of the coprecipitated $Cu_{0.5}[Ce(La)]_{0.5}O_x$ catalyst. A large number of bulk CuO particles were found with this sample. It is interesting to note that the bulk CuO particles were typically covered by the smaller cerium oxide particles. However, an even distribution of copper clusters on cerium oxide, similar to Fig. 3d for the nitric-acid-treated $Cu_{0.15}[Ce(La)]_{0.85}O_x$ catalyst, was found in an area mainly consisting of the cerium oxide particles. These copper clusters did not appear in Fig. 3e because of their very small intensity relative to bulk CuO particles. Figure 3f shows the elemental map of the $Cu_{0.01}[Ce(La)]_{0.99}O_x$ catalyst prepared by coprecipitation and 4 h calcination at 600°C in N_2. As expected, copper in this catalyst was well dispersed in the cerium oxide and its distribution pattern exactly matched that of cerium, which suggests the formation of a solid solution. Note that the high copper dispersion area in Fig. 3f represents a uniform copper distribution rather than a high copper content. Heating the $Cu_{0.01}[Ce(La)]_{0.99}O_x$ catalyst in flowing air at 860°C drove the copper from the bulk to the surface and caused copper atoms to aggregate into clusters. Resulting elemental maps looked similar to that of the nitric-acid-treated $Cu_{0.15}[Ce(La)]_{0.85}O_x$ catalyst but had a less dense copper cluster population.

Since the coprecipitated catalysts contained lanthanum impurity, the X-ray probe was also used to check for La distribution. The analyses indicated an atomic level mixing of lanthanum with cerium oxide or the formation of solid solution. No lanthanum association with copper was found. The overall STEM analysis results are now summarized as: (i) copper in small amounts (a few percent) has a strong tendency to associate with cerium oxide irrespective of the catalyst preparation method; (ii) excess copper forms bulk CuO particles that were covered by smaller CeO_2 particles; and (iii) heating the catalyst of atomic copper dispersion caused the segregation of copper and the formation of copper clusters.

3.1.3. XPS analyses of the Cu–Ce–O catalyst system. In the preceding paper (1) we reported the catalyst surface composition as measured by XPS. Here, the

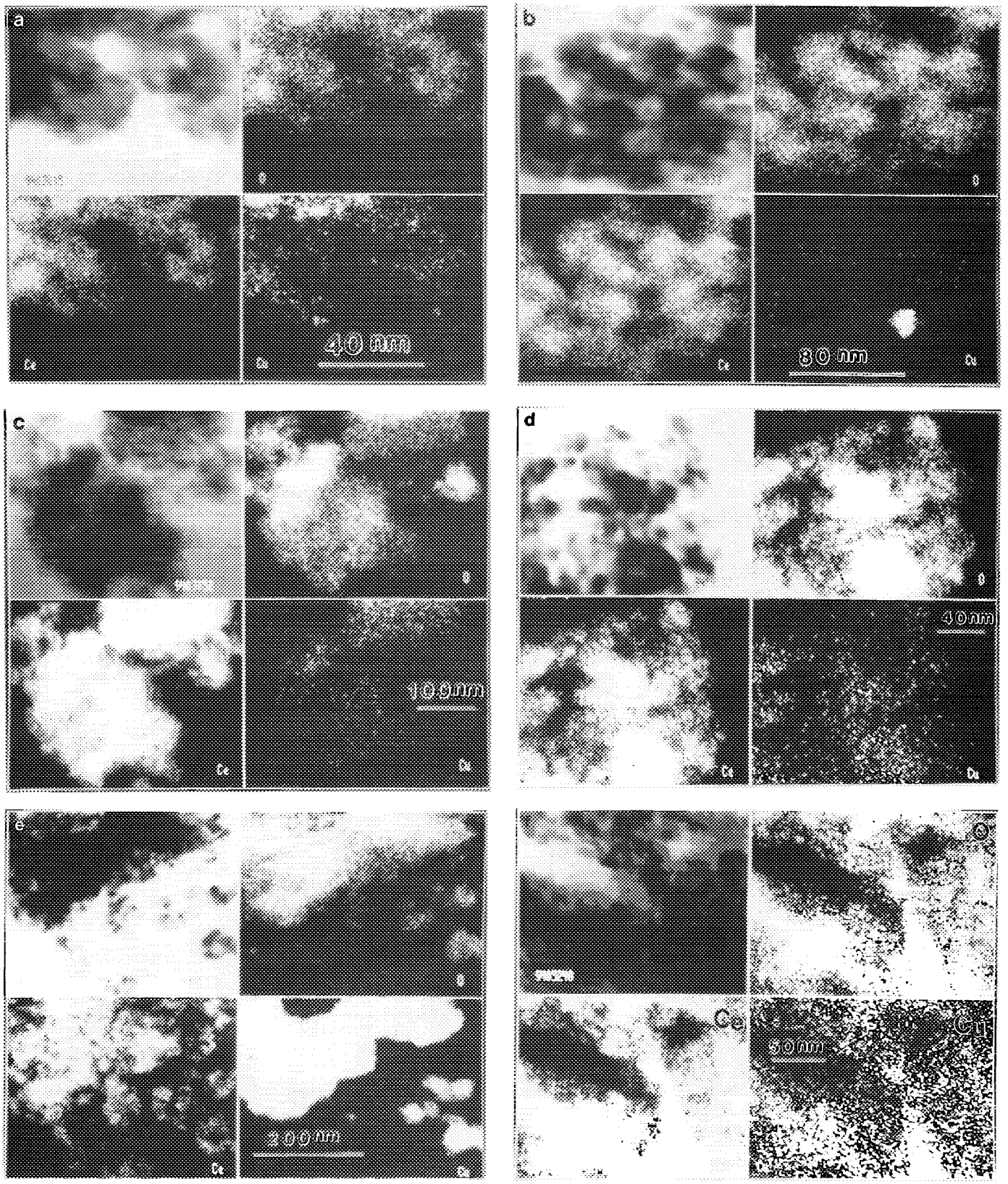

FIG. 3. (a) STEM/EDX elemental maps of the $Cu_{0.15}[Ce(La)]_{0.85}O_x$ catalyst prepared by coprecipitation; (b) STEM/EDX elemental maps of the 15 at.% $CuOx/CeO_2$ catalyst prepared by impregnation; (c) STEM/EDX elemental maps of the 15 at.% $CuO + CeO_2$ catalyst prepared by mixing; (d) STEM/EDX elemental maps of the $Cu_{0.15}[Ce(La)]_{0.85}O_x$ catalyst treated by nitric acid; (e) STEM/EDX elemental maps of the $Cu_{0.5}[Ce(La)]_{0.5}O_x$ catalyst prepared by coprecipitation; and (f) STEM/EDX elemental maps of the $Cu_{0.01}[Ce(La)]_{0.99}O_x$ catalyst prepared by coprecipitation (4-h calcination under N_2 at 600°C).

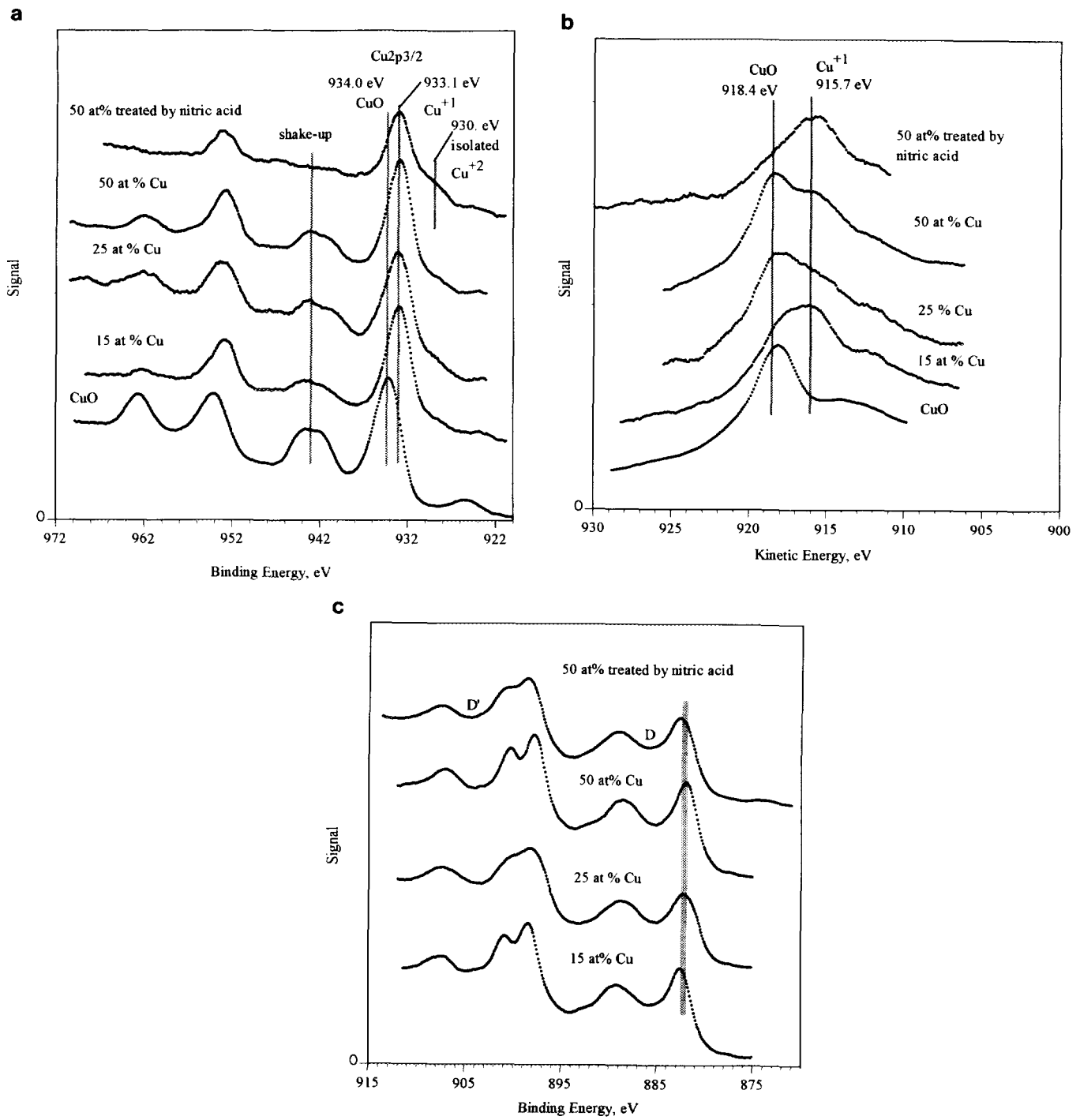

FIG. 4. (a) Cu2p XP spectra of Cu–Ce(La)–O catalysts of high copper content (prepared by coprecipitation). (b) kinetic energy spectra of the Auger L_3VV electron of the Cu–Ce(La)–O catalysts; and (c) Ce3*d* XP spectra of the Cu–Ce(La)–O catalysts.

detailed XP spectra are presented. We found that the XP spectra of the Cu–Ce(La)–O sample were unstable in the high vacuum chamber (ca. 7×10^{-8} Torr) during the initial period of measurement. Once the sample was introduced into the XPS chamber, the relative intensity of the $Cu2p_{3/2}$ shake-up peak at 943 eV slightly decreased with on-stream measurement time while the $Cu2p_{3/2}$ peak position shifted toward a lower binding energy from 934.0 eV. However, the XP spectra became stable after about 30 min. The shake-up peak and higher $Cu2p_{3/2}$ binding energy are two major XPS characteristics of CuO, while the lower $Cu2p_{3/2}$ binding energy and absence of the shake-up peak are characteristic of reduced copper species (16). It is known that supported-copper oxide can be reduced by

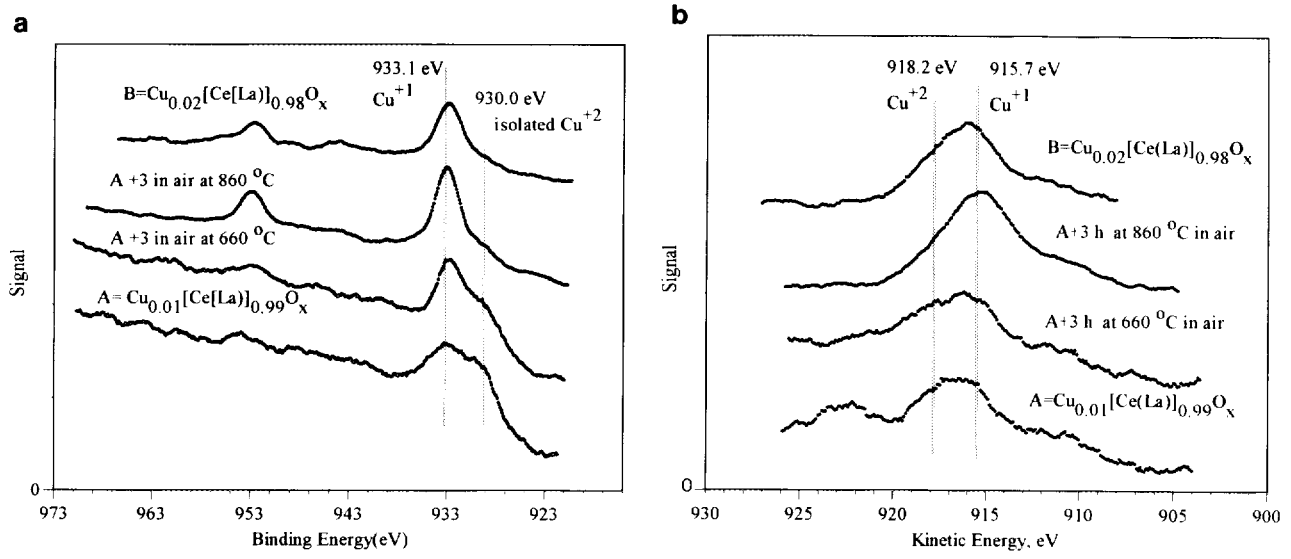

FIG. 5. (a) Cu2*p* XP spectra of $Cu_{0.01}[Ce(La)]_{0.99}O_x$ and $Cu_{0.02}[Ce(La)]_{0.98}O_x$ catalysts ($Cu_{0.01}[Ce(La)]_{0.99}O_x$ prepared by 4-h calcination under N_2 at 600°C; $Cu_{0.02}[Ce(La)]_{0.98}O_x$ prepared by 4-h calcination at 650°C plus 3-h calcination at 860°C, both in air); (b) kinetic energy spectra of the Auger L_3VV electron of the $Cu_{0.01}[Ce(La)]_{0.99}O_x$ and $Cu_{0.02}[Ce(La)]_{0.98}O_x$ catalysts.

the X-ray beam during XPS analysis. Although the beam effect could not be eliminated in the present XPS apparatus, further work confirmed that the initial instability of the Cu–Ce(La)–O sample was not suppressed by decreasing the X-ray power and was likely caused by the desorption of weakly bound surface oxygen under high vacuum. Figures 4a–4c show the XPS analyses of the 15, 25, and 50 at.% Cu–Ce(La)–O catalysts prepared by coprecipitation. These data were acquired in the Multiplex mode with about 1-h total acquisition time. Bulk CuO was prepared by thermal decomposition of copper carbonate and used as reference.

In Fig. 4a, the bulk CuO shows a strong shake-up peak; the shake-up peak intensity of the Cu–Ce(La)–O catalysts increased with the copper content and disappeared after the catalyst was treated by nitric acid using the procedure described previously. The Cu2$p_{3/2}$ peak of the bulk CuO was centered at 934.0 eV, while the same peaks of the Cu–Ce(La)–O catalysts were centered at about 933.1 eV. The present observations suggest both CuO and reduced copper species existing in these Cu–Ce(La)–O catalysts. We could deconvolute the Cu2$p_{3/2}$ peak to find the relative proportion of CuO in the Cu–Ce(La)–O catalysts, but this peak did not show an apparent doublet shape, which made it hard to obtain a reliable value from this mathematical process. In addition, the weak shake-up peak did not allow us to use the shake-up peak/peak ratio for a reliable estimation either. Therefore, our discussion of the XPS results will be qualitative.

The two possible reduced copper forms, namely, metallic copper and Cu_2O, have similar binding energies but different Auger parameters (16–20). Figure 4b shows the kinetic energy spectra of the Auger L_3VV electron. The doublet peaks for the Cu–Ce(La)–O samples also suggest the presence of two copper species. The 918.4 and 915.7 eV peaks in the Auger kinetic spectra correspond to bulk CuO and Cu^+ species, respectively. In agreement with the literature data we then assign the Cu2$p_{3/2}$ peak at higher binding energy (934.0 eV) to CuO and the Cu2$p_{3/2}$ peak at the lower binding energy (933.1 eV) to the Cu^+ species (Fig. 4a). Figure 4c shows the Ce3*d* XP spectra for the four catalyst samples under study. The four spectra look basically the same and look similar to the spectra of bulk CeO_2 reported in the literature (16). The binding energies for bulk CeO_2 and reduced cerium oxide are the same, but small spikes or peaks are usually found in the reduced cerium oxide at the D and D′ positions (21, 22).

Figures 5a and 5b show the Cu2*p* XP spectra and L_3VV kinetic energies of the $Cu_{0.01}[Ce(La)]_{0.99}O_x$ and $Cu_{0.02}[Ce(La)]_{0.98}O_x$ catalysts. No shake-up peak was observed in Fig. 5a, while the Cu2$p_{3/2}$ peak was deconvoluted into two components: one at 933.1 eV and another at 930.0 eV. The first was assigned to Cu^+ species. The second component was difficult to assign since no copper species with such a low binding energy has been reported in the literature. We postulate that this component is due to isolated Cu^{2+} ions in the cerium oxide lattice. The existence of isolated copper ions and ion pairs in the Cu–Ce–O system was reported by Abou Kais *et al.* (23, 24) and Sorial *et al.* (25), both using the electron paramagnetic resonance technique. The fraction of Cu^+ species in Fig. 5a increased with heating temperature, while the fraction of isolated Cu^{2+} ions decreased. The STEM analyses indi-

cated that heating the $Cu_{0.01}[Ce(La)]_{0.99}O_x$ catalyst in air drove the isolated copper ions to form copper clusters. Two components seem to exist in the kinetic energy spectra of the Auger L_3VV electron in Fig. 5b. It is noted that the isolated copper component at 930.1 eV also appeared in the XP spectra for the nitric-acid-treated 50 at.% copper-containing sample shown in Fig. 4a. This was probably due to the copper ions remaining on the cerium oxide surface after the sample had been immersed in nitric acid for 14 h.

The XRD, STEM, and XPS analysis results for the Cu–Ce–O catalysts are briefly summarized as follows: (i) copper clusters undetectable by XRD exist in all the Cu–Ce–O catalysts and the relative amount of copper depends on catalyst preparation, composition, and thermal treatment; and (ii) the Cu^+ species result from the strong interaction of the copper clusters with cerium oxide.

3.2. Kinetic Results

3.2.1. CO oxidation kinetics over the $Au_{0.05}[Ce(La)]_{0.95}O_x$ catalyst. Figure 6 shows the variation of CO oxidation rate on the $Au_{0.05}[Ce(La)]_{0.95}O_x$ catalyst with the partial of pressure of CO (P_{CO}) and oxygen (P_O). The experimental data were best fitted by a power order equation [2], with $m = 0.30$ and $n = 0.18$

$$R_{co} = kP_{co}^m P_o^n. \quad [2]$$

The R^2 values given in Fig. 6 indicate that the plots of the rate versus P_{CO} under constant P_O were generally better fitted than the plots of the rate versus P_O. This is due to the lower reaction order in P_O. Although difficult to regress, this function is not important because of its small contribution to the overall rate process. The Arrhenius plot of the rate constant, k, is shown in Fig. 9. The apparent activation energy was 53.7 kJ/mol. The reaction orders and activation energy are compared to the literature data for other gold–metal oxide catalysts in Table 1. The $Au_{0.05}[Ce(La)]_{0.95}O_x$ catalyst showed similar kinetics to the other gold catalysts but had a higher activation energy and a stronger dependence on the partial pressure of CO.

TABLE 1

CO Oxidation Kinetics over Au–Oxide Catalysts

Catalysts	Au size (nm)	m	n	E_{app} (kJ/mol)
$Au_{0.05}[Ce(La)]_{0.95}O_x$[a]	8.0	0.30	0.18	53.7
$Au–Fe_2O_3$ (14)	4.0	0.00	0.05	35.0
$Au–TiO_2$ (14)	2.0	0.05	0.24	34.2

[a] Catalyst was prepared by calcination in air: 1 h at 500°C + 1 h at 600°C.

3.2.2. CO oxidation kinetics over the Cu–Ce–O catalysts. The $Cu_{0.15}[Ce(La)]_{0.85}O_x$ catalyst and the $Cu_{0.01}[Ce(La)]_{0.99}O_x$ catalyst subjected to different thermal treatments were chosen for the kinetic study in order to also examine the composition effect. Figures 7 and 8 show the

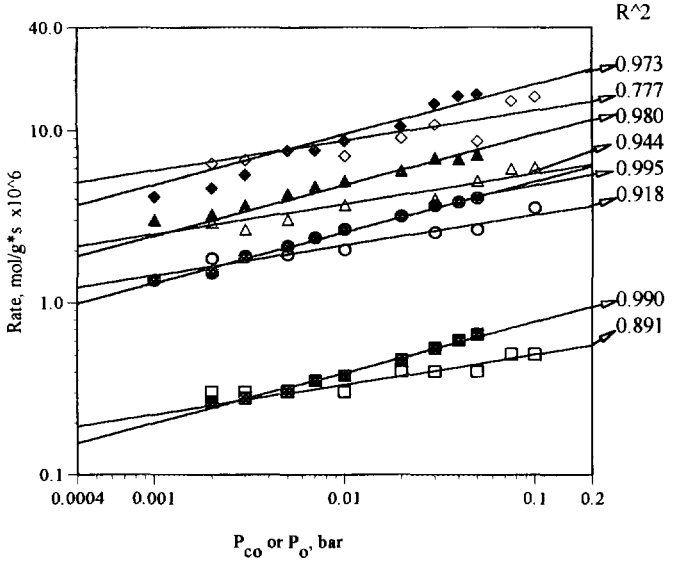

FIG. 6. Variation of CO oxidation rate over the $Au_{0.05}[Ce(La)]_{0.95}O_x$ catalyst with partial pressure of oxygen and CO (R is the correlation coefficient); closed symbols for P_{CO} under $P_O = 0.05$ and open symbols for P_O under $P_{CO} = 0.01$; (■) 10°C; (●) 25°C; (▲) 43°C; and (◆) 54°C.

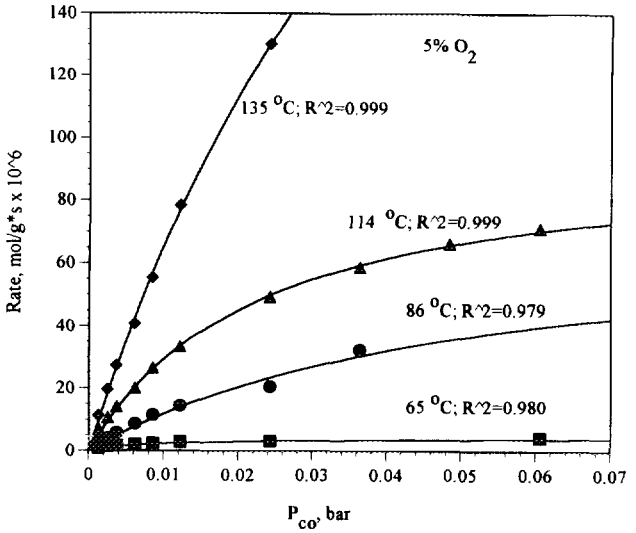

FIG. 7. Variation of CO oxidation rate over the $Cu_{0.15}[Ce(La)]_{0.85}O_x$ catalyst with partial pressure of CO under constant P_O (R is the correlation coefficient).

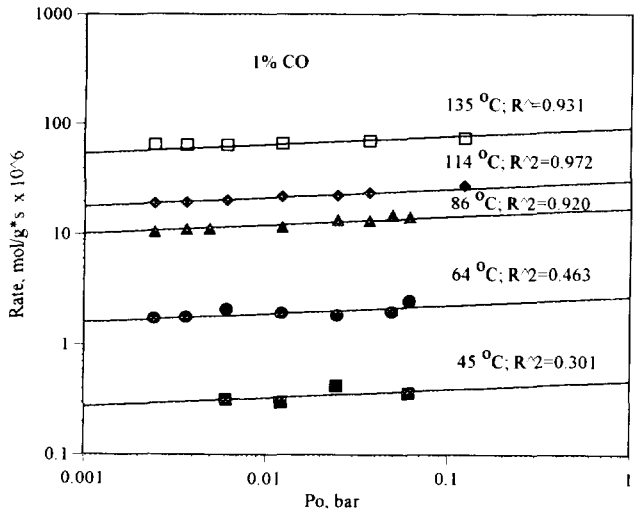

FIG. 8. Variation of CO oxidation rate over the $Cu_{0.15}[Ce(La)]_{0.85}O_x$ catalyst with partial pressure of oxygen under constant P_{CO} (R is the correlation coefficient).

variation of the CO oxidation rates on the $Cu_{0.15}[Ce(La)]_{0.85}O_x$ at different reaction temperatures with P_{CO} and P_O, respectively. Under constant P_O, the rate increased with P_{CO}. The reaction order in P_{CO} seems to decrease from one to zero as P_{CO} increases. In Fig. 8 the rate slowly increased with P_O under constant P_{CO}. Various rate equations derived from different reaction mechanisms as well as the empirical power order equation [2] were evaluated to regress the experimental data. It was found that the experimental data were best represented by the equations

$$R_{CO} = \frac{k_{co} K_{co} P_o^n}{1 + K_{co} P_{co}} \quad [3]$$

$$k_{CO} = A \exp(-E_a/RT) \quad [4]$$

$$K_{CO} = K \exp(Q/RT). \quad [5]$$

The parameters k_{CO} and K_{CO} in Eq. [3] can be taken as the surface reaction rate constant and CO adsorption equilibrium constant, respectively. The Arrhenius plots of k_{CO} and K_{CO} are shown in Fig. 9 from which the reaction activation energy and heat of adsorption were obtained.

The experimental data for the $Cu_{0.01}[Ce(La)]_{0.99}O_x$ catalysts were also best regressed by Eq. [3]. The Arrhenius plots of the resulting constants are shown in Fig. 10. The values of those parameters in Eqs. [4] and [5] for all the Cu–Ce(La)–O catalysts are listed in Table 2. The reaction orders in P_O, n, are small numbers close to zero. The activation energy is in the range of 73 to 94 kJ/mol while the heat of CO adsorption is in the range of 28 to 61 kJ/mol. Some interesting results were observed with the $Cu_{0.01}[Ce(La)]_{0.99}O_x$ catalyst. Heating this catalyst at 860°C in air changed the negative reaction order of P_O to positive and increased the preexponential factor of the reaction constant k_{CO} and the heat of adsorption. This increase corresponds to the increase in copper cluster population and Cu^+ fraction as we found from the STEM and XPS analyses. The last column in Table 2 shows the apparent activation energy when $K_{CO}P_{CO} \ll 1$. Under this condition, the reaction rate becomes first-order in P_{CO} and the apparent activation energy is $E_a - Q$. Table 2

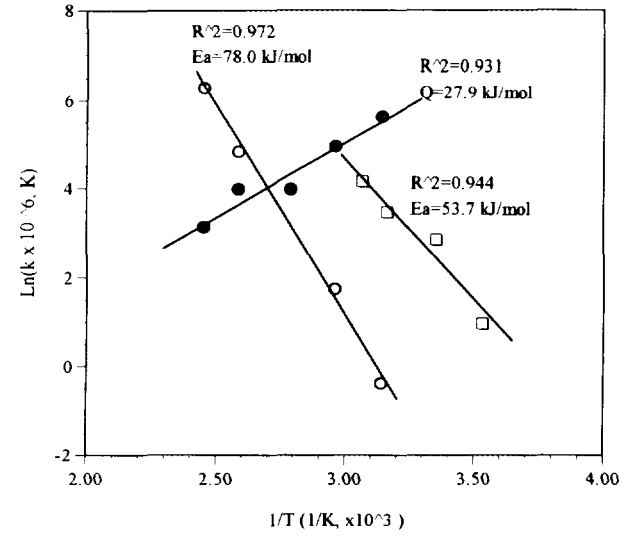

FIG. 9. Arrhenius plots of constants k and K for CO oxidation over $Au_{0.05}[Ce(La)]_{0.95}O_x$ and $Cu_{0.15}[Ce(La)]_{0.85}O_x$ catalysts (R is the correlation coefficient); (□) k for $Au_{0.05}[Ce(La)]_{0.95}O_x$; (○) k_{CO} for $Cu_{0.15}[Ce(La)]_{0.85}O_x$; (●) K_{CO} for $Cu_{0.15}[Ce(La)]_{0.85}O_x$.

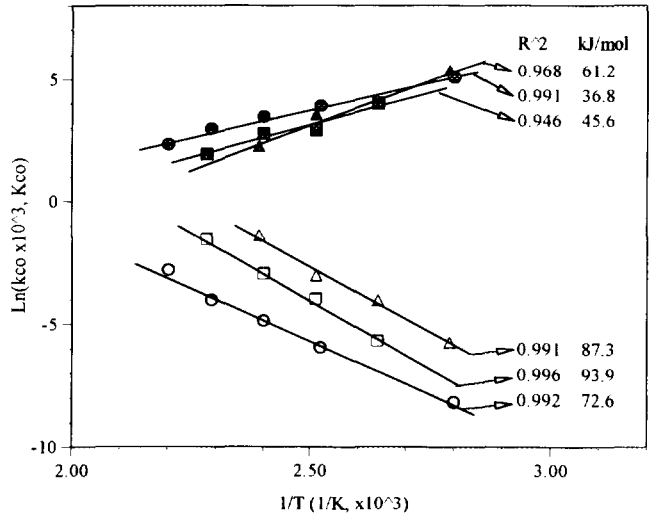

FIG. 10. Arrhenius plots of constants k_{CO} and K_{CO} for CO oxidation over $Cu_{0.01}[Ce(La)]_{0.99}O_x$ catalysts (R is the correlation coefficient); open symbols for k_{CO} and closed symbols for K_{CO}; (○) fresh; (□) +3 h at 650°C; (△) +3 h at 860°C.

TABLE 2

CO Oxidation Kinetics over the Cu–Ce(La)–O and Other Copper Catalysts

Catalyst	n	A (mol/g · s · bar^n)	E (kJ/mol)	K (1/bar)	Q (kJ/mol)	E_{app}[a] (kJ/mol)
$Cu_{0.15}[Ce(La)]_{0.85}O_x$[b]	0.08 ± 0.03	5.91×10^6	78.0	6.47×10^{-3}	27.9	50.1
$Cu_{0.01}[Ce(La)]_{0.99}O_x$						
Fresh[c]	−0.09 ± 0.02	9.82×10^3	72.7	6.82×10^{-4}	36.8	35.9
+Heated 3 h at 660°C[d]	0.0 ± 0.07	3.23×10^7	93.9	2.49×10^{-5}	45.6	48.3
+Heated 3 h at 860°C[d]	0.12 ± 0.02	1.78×10^7	87.3	2.50×10^{-7}	61.2	26.1
$CuO–Cr_2O_3/\gamma$-Al_2O_3 (26) (Cu : Cr = 1 : 1) 10 wt%	0	2.96×10^2	91.0	7.5×10^{-2}	5.0	86
12 wt% Cu/δ-Al_2O_3 (27)	—	—	90–110	—	~30.1	—

[a] $E_{app} = E_a - Q$, corresponding to the kinetic equation $kK_{CO}P_{CO}P_O^n$ when $K_{CO}P_{CO} \ll 1$.
[b] Calcined in air, 4 h at 650°C.
[c] Calcined under N_2, 4 h at 600°C.
[d] In flowing air.

also includes kinetic data for other copper catalysts from the literature for comparison. The $CuO–Cr_2O_3/\gamma$-Al_2O_3 catalyst, precalcined in air at 500°C (26), gave a preexponential factor of the constant k_{CO} four orders of magnitude lower than those of the Cu–Ce(La)–O catalysts and also gave a low heat of adsorption (5 kJ/mol). High heat of adsorption (30 kJ/mol) was reported for the Cu/δ-Al_2O_3 catalyst prereduced by H_2 at 300°C (27). It is noted that we calculated the data in Table 2 for the $CuO–Cr_2O_3/\gamma$-Al_2O_3 catalyst based on the reported rate equation in the literature (26).

Because of the variations in both the preexponential factor and activation energy of the rate constant in Table 2, it is difficult to evaluate the effect of the copper content on the reaction kinetics. In Fig. 11, the rate constant k_{CO} normalized by the BET surface area is plotted versus the surface copper content (at.%) as measured by XPS. One can see that the rate constant k_{CO} steeply increases with the surface copper content. The plots for three different reaction temperatures are well regressed by the same power order equation

$$k_{co}/S_g \propto S_{Cu}^{3.4}, \qquad [6]$$

where S_g is the catalyst surface area (m^2/g), and S_{Cu} is the surface copper content. Although we cannot find a mechanistic explanation for such a relationship at the present time, the highly nonlinear correlation suggests a complex interaction of copper and cerium oxide. The high catalytic activity did not result from copper dispersion alone. One can extrapolate that k_{CO} will increase by an order of magnitude if the surface copper content is further increased from 25 to 40%. However, we could not achieve a surface copper level higher than ca. 25 at.% in this work. Figure 12 shows that the catalyst surface was enriched in copper for low bulk copper content and reached a plateau for high bulk copper content. The 24.8 at.% for the $Cu_{0.15}[Ce(La)]_{0.85}O_x$ is the largest surface copper content reached by a series of Cu–Ce–O catalysts prepared by 4 h of calcination at 650°C. The surface copper level of the $Cu_{0.15}[Ce(La)]_{0.85}O_x$ was not increased by reduction in 25% H_2/He or by heating in air. The impregnation method did not increase the copper level either. The main reason, based on the catalyst characterization results, is that an excess amount of copper over a certain value favored the agglomeration of copper in bulk CuO form. Bulk CuO particles were then covered by fine cerium oxide particles and could not be detected by XPS.

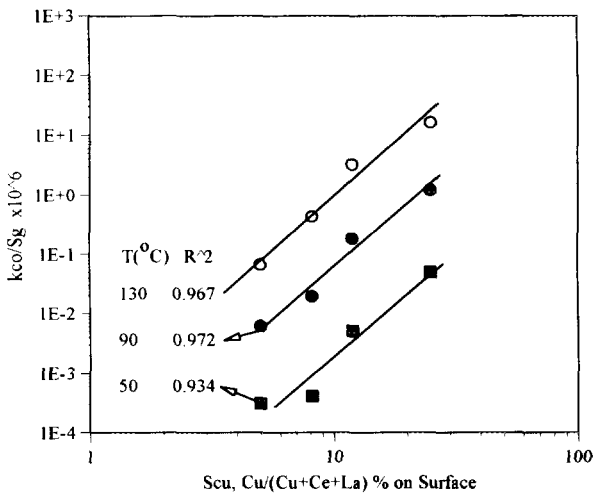

FIG. 11. Variation of normalized reaction rate constant (k_{CO}/S_g) for CO oxidation over the Cu–Ce(La)–O catalysts with the surface copper fraction (R is the correlation coefficient).

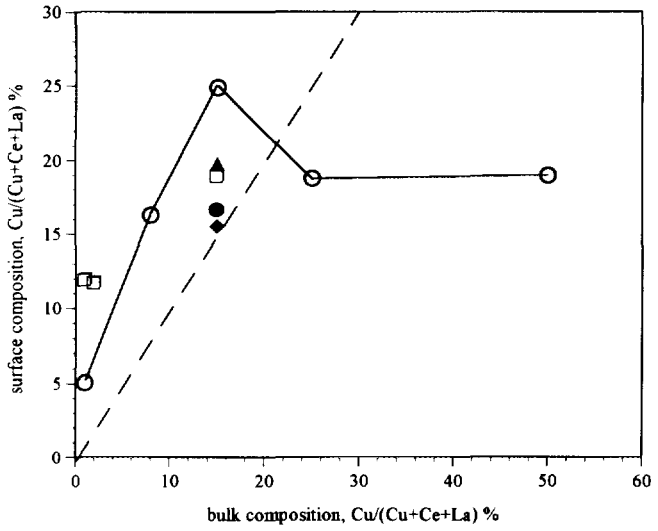

FIG. 12. Variation of the surface copper fraction of the Cu–Ce(La)–O catalyst with bulk composition and thermal treatment; (○) as prepared by 4-h calcination at 650°C in air; (□) further heated for 3 h in flowing air at 860°C; (▲) reduced by 25% H_2/He for 2 h at 300°C; (◆) reduced by 25% H_2/He for 1 h at 600°C; (●) prepared by impregnation.

3.2.3. Methane oxidation. Figures 13 and 14 show the variation of the methane oxidation rate over the $Cu_{0.15}[Ce(La)]_{0.85}O_x$ catalyst with the partial pressure of methane and oxygen, respectively. The reaction kinetics were similar to the CO oxidation. Thus, the experimental data were best fitted by Eq. (7). The Arrhenius plots of the constants k_m and K_m in this equation are shown in Fig. 15, from which Eqs. [8] and [9] were derived:

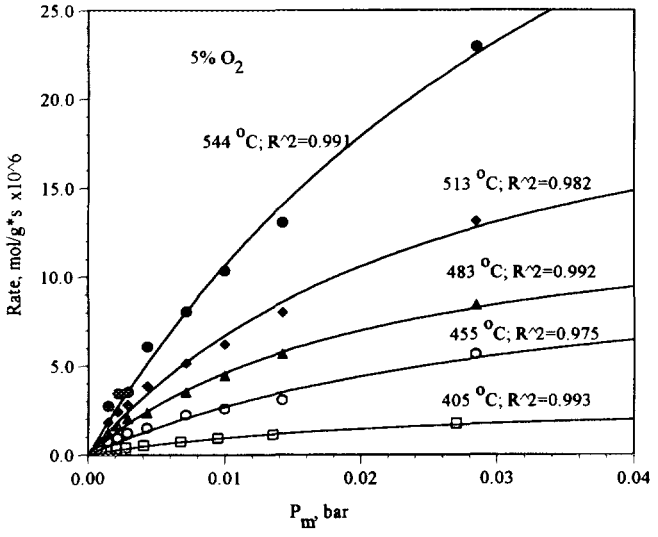

FIG. 13. Variation of methane oxidation rate over the $Cu_{0.15}[Ce(La)]_{0.85}O_x$ catalyst with partial pressure of methane under constant P_O (R is the correlation coefficient).

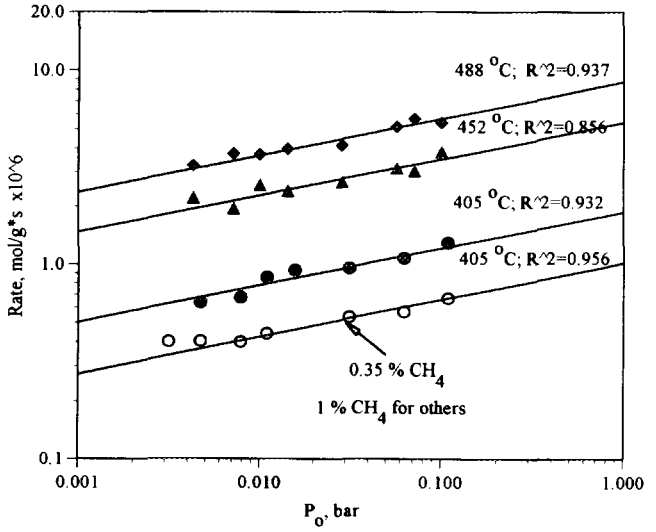

FIG. 14. Variation of methane oxidation rate over the $Cu_{0.15}[Ce(La)]_{0.85}O_x$ catalyst with partial pressure of oxygen under constant P_m (R is the correlation coefficient).

$$R_m = \frac{k_m K_m P_m P_O^{0.18\pm0.04}}{1 + K_m P_m} \quad [7]$$

$$k_m = 7.84 \times 10^1 \exp(-93.4 \times 10^3/RT) \quad [8]$$

$$K_m = 3.46 \exp(-14.2 \times 10^3/RT). \quad [9]$$

The plot of K_m data versus $1/T$ in Fig. 15 shows an abrupt change between 1.37×10^{-3} and 1.32×10^{-3} in $1/T$ axis (corresponding to 455 and 483°C) resulting in a low correlation coefficient. We could have divided the

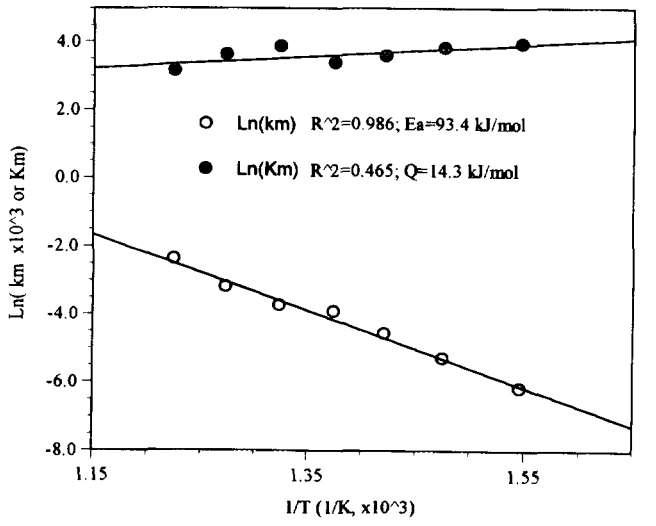

FIG. 15. Arrhenius plots of constants k_m and K_m for methane oxidation over $Cu_{0.15}[Ce(La)]_{0.85}O_x$ catalyst (R is the correlation coefficient).

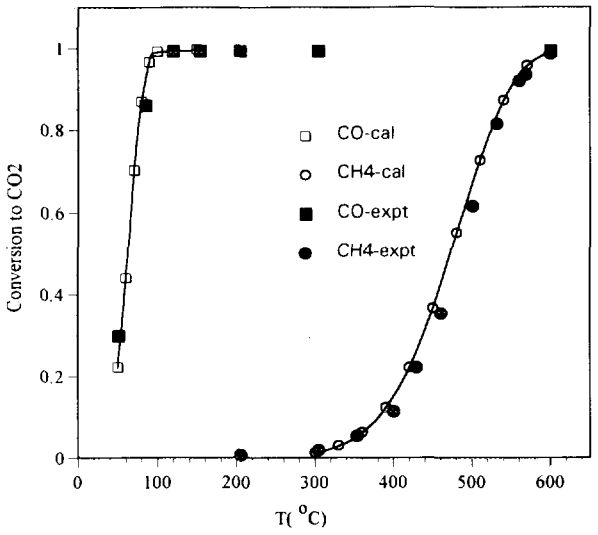

FIG. 16. Comparison of calculated light-off curves with experimental data ($Cu_{0.15}[Ce(La)]_{0.85}O_x$ catalyst; 0.09 g · s/cc (STP); 0.228% CH_4, 0.1% CO, 1% O_2).

data into two regions to achieve better curve-fitting. Considering, however, the overall small variation in K_m, we preferred to use the single Arrhenius equation as a crude approximation.

3.2.4. Verification of kinetic equations. Since the above kinetic models for both the CO and methane oxidation were obtained with experimental data measured in a differential reactor mode, the question as to whether the rate equations are valid at high conversions was considered next. We calculated the light-off curves for the simultaneous oxidation of CO and methane over the $Cu_{0.15}[Ce(La)]_{0.85}O_x$ catalyst for a gas mixture of 0.1% CO, 0.228% CH_4, and 1% O_2 at a contact time of 0.09 s · g/cc. We did not detect any axial temperature gradient under these reaction conditions because of the small reactor diameter and shallow packed catalyst bed. Therefore, CO conversion at each temperature was calculated by integrating the equation

$$\frac{N_t \cdot dP_{CO_2}}{P \cdot dW_{cat}} = \frac{k_{CO} K_{CO} P_{CO} P_O^{0.08}}{1 + K_{CO} P_{CO}} \qquad [10]$$

$$P_{CO_2} = (P_{CO})_{inlet} - P_{CO}, \qquad [11]$$

where N_t is the total gas flow rate, P is the total pressure and is assumed to be constant when a dilute reacting gas is used, and W_{cat} is the catalyst weight. Methane conversion was calculated in exactly the same manner. The calculated light-off curves in Fig. 16 are in excellent agreement with experimental data. It is noteworthy that the kinetic model was developed based on individual reaction data while the experimental data were for the simultaneous oxidation of CO and methane. This indicates that oxidation of CO and methane are independent reactions.

4. DISCUSSION

4.1. CO Oxidation over the $Au_{0.05}[Ce(La)]_{0.95}O_x$ Catalyst

The $Au_{0.05}[Ce(La)]_{0.95}O_x$ catalyst characterization revealed that gold was distributed in the cerium oxide matrix as distinct metallic particles. There was no evidence of strong interaction between the gold particles and cerium oxide. It is known that neither cerium oxide nor gold alone is an active CO oxidation catalyst. The enhanced activity was solely due to the synergistic effect of the two kinds of materials. Extensive studies of gold/oxide catalysts were reported by Haruta *et al.* (14). The Au–Ce–O is a new catalyst system, but we propose a reaction mechanism similar to that for other gold/oxide catalysts (14), as illustrated in Fig. 17.

In this model, CO molecules adsorb on the gold particle surface, while oxygen molecules adsorb on the metal oxide surface. Then, the two adsorbed species react at the boundary of the gold and metal oxide. The highly active sites created at the boundary provide quick turnover of reacting species and high reaction activity. The adsorbed CO on the gold particle and the surface oxygen on the metal oxide may move to the boundary area by surface diffusion. Apparently, decreasing gold particle size will increase the boundary area and thus, the catalytic activity. The kinetic results in Table 1 show that the rate on the $Au_{0.05}[Ce(La)]_{0.95}O_x$ catalyst had stronger dependence on the partial pressure of the reacting species and higher activation energy than those on the other gold/oxide catalysts (14). The present catalyst, prepared by calcination in air for 1 h at 500°C + 1 h at 640°C, comprised larger gold particles (8 nm). The larger gold particles resulted in a lower interfacial area and slower diffusion of the reacting species on the surface.

The high activity of the $Au_{0.05}[Ce(La)]_{0.95}O_x$ catalyst clearly demonstrated the synergistic effect of dual function materials in the CO oxidation. It is known that water vapor inhibits CO adsorption on cerium oxide. CO oxidation on the $Au_{0.05}[Ce(La)]_{0.95}O_x$ catalyst was not affected by water vapor, further suggesting the role which gold plays in providing CO adsorption sites. The role of cerium

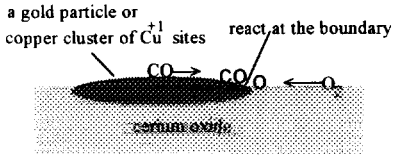

FIG. 17. Synergistic reaction model for CO oxidation over the Au–Ce–O and Cu–Ce–O catalysts.

oxide in supplying oxygen will be discussed in the next section together with the CO oxidation on the Cu–Ce–O catalyst.

4.2. *CO Oxidation over the Cu–Ce(La)–O Catalyst*

On base metal oxide catalysts (26–28), the CO oxidation rate generally has a weak dependence on P_O and has a positive order from 0 to 1 in P_{CO}. The kinetic behavior of the Cu–Ce(La)–O catalyst is overall similar to that of the base metal oxide catalysts. Both the Eley–Rideal and Langmuir–Hinshelwood models have been proposed for CO oxidation on the copper-based catalysts. Dekker *et al.* (26) developed a comprehensive kinetic model for CO oxidation over the $CuO–Cr_2O/\gamma\text{-}Al_2O_3$ catalyst based on a Eley–Rideal model consisting of several elementary steps. With *in situ* IR measurements of CO oxidation on the $Cu/\delta\text{-}Al_2O_3$ catalyst, Choi and Vannice (27) revealed a clear first-order dependence of the reaction on chemisorbed CO and the absence of activity when no adsorbed CO was detected. This different conclusion was underlined by the difference in catalyst pretreatment and reaction conditions. Copper was in a partially oxidized state in the $Cu/\delta\text{-}Al_2O_3$ catalyst but was likely to be in a fully oxidized state in the $CuO–Cr_2O_3/\gamma\text{-}Al_2O_3$. Jernigan and Somorjai (18) recently compared the CO oxidation over three different oxidation states of copper, Cu, Cu_2O, and CuO, and found that the apparent activation energy increases with increasing copper oxidation state ($Cu(37.6) < Cu_2O(58.5) < CuO(71.1)$). The apparent activation energy listed in Table 2 for the Cu–Ce(La)–O catalysts is in the range of 26 to 50 kJ/mol, similar to the reduced copper oxide.

The unique information conveyed by Table 2 is the high heat of CO adsorption over the Cu–Ce(La)–O derived from the kinetic measurements, which is comparable to that of CO adsorption on metallic copper, 30 to 68 kJ/mol as reported in the literature (29, 30). Note that the heat of CO adsorption over the precalcined $CuO–Cr_2O_3/\gamma\text{-}Al_2O_3$ catalyst is indeed a small number. This may be the reason that CO has been assumed not to adsorb on the CuO surface. Recall that Cu^+ species for the Cu–Ce(La)–O catalyst were observed by XPS. We believe that the Cu^+ surface species provide strong CO adsorption sites and that CO oxidation over the Cu–Ce(La)–O catalyst proceeds via the Langmuir–Hinshelwood mechanism.

Given the fact that the present Cu–Ce(La)–O catalyst was typically prepared by a few hours-long calcination at temperatures of at least 650°C in air and was used for kinetic studies without any prereduction treatment, how are the Cu^+ species stabilized? We propose that the copper ions at the interfacial area of a copper cluster and cerium oxide can penetrate into the cerium oxide lattice

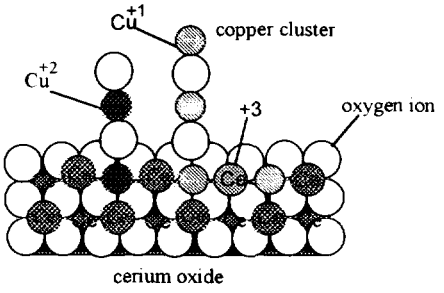

FIG. 18. Interaction model of copper with cerium oxide (cross section of ceria showing a [001] plane of oxygen ions and adjacent cerium cations).

by occupying the vacant sites of cerium ions as illustrated by Fig. 18. The copper ionic size found in the literature varies among different sources. However, it is agreed that Cu^+ ion size is larger than the Cu^{2+}. The Cu^+ species is more compatible in cerium oxide lattice in terms of the size. Thus, Cu^+ is stabilized by the cerium oxide lattice and transferred to the outer surface by a copper oxide chain, $Cu^+–O–Cu–\cdots–O–Cu^+$. The reducibility of Ce^{4+} to Ce^{3+} enhances the flexibility of a copper ion to adapt to a different oxidation state by maintaining the electronic neutrality of the lattice. The existence of isolated Cu^{2+} ions and ion pairs in the cerium oxide lattice was studied with the electron paramagnetic resonance technique (23–25), but this technique cannot detect the Cu^+ species. The formation of chemical bonding between the copper clusters and cerium oxide explains the strong association of copper with cerium oxide as found in catalyst preparation and activity tests.

In addition to the strong CO adsorption, the reaction rate on the Cu–Ce(La)–O catalysts was several orders of magnitude higher than that on either the oxidized $CuO–Cr_2O_3/\gamma\text{-}Al_2O_3$ or the reduced $Cu/\delta\text{-}Al_2O_3$ catalyst. We propose a reaction model for CO oxidation over the Cu–Ce(La)–O catalyst similar to the Au/metal oxide system with the Cu^+ species of the copper cluster replacing gold particles and providing surface sites for CO adsorption. Given the catalyst configuration in Fig. 17, a minute Schottky junction can form at the interface between metals and oxides and affect the electronic properties of metal oxides (31). However, it has always been difficult to relate the catalyst electronic property to catalytic activity. We rather attribute the enhanced catalytic activity to the concerted effect of CO adsorption and oxygen activation. Cerium oxide can provide various active surface oxygen species for oxidation reactions. The surface oxygen species on cerium oxide were studied by TPR (32), FTIR (33, 34), and EPR (35). The possible oxygen species are shown in Eq. [12]. Generally, increasing the catalyst treatment temperature shifts the equilibrium to the right, that is, the lattice oxygen will be a major component if heated

at high temperatures

$$O_2 \leftrightarrow O_2^- \leftrightarrow O_2^{2-} \leftrightarrow O^- \leftrightarrow O^{2-}_{\text{lattice}}. \quad [12]$$

A superoxide species (O_2^-) forms from the adsorption of an oxygen molecule on a single unsaturated surface cerium ion ($Ce^{+4} \cdots O_2^-$). The formation of peroxide species (O_2^{2-}) increases with the extent of reduction of the cerium oxide surface. The peroxide species is probably associated with a pair of reduced cerium ions or one oxygen vacancy. The superoxide species has a very quick exchange rate with gaseous oxygen at low temperatures (below 100°C) according to Li *et al.* (34, 36). It is also labile on the cerium oxide surface and its surface diffusion is much faster than on SiO_2 or Al_2O_3 (37). Therefore, we propose the superoxide species as the active surface oxygen species in CO oxidation over both the Au–Ce(La)–O and Cu–Ce(La)–O catalysts, according to the reaction model in Fig. 17. In fact, oxygen spillover and reaction with CO at the interface were demonstrated by Metcalfe and Sundaresan with the Pt/YSZ catalyst (10). Tarasov *et al.* (38) proposed that the junction effect between the precious metals and cerium oxide facilitates the formation of superoxide species. This argument is applicable to the Au–Ce(La)–O catalyst where distinctive metallic gold particles were identified. In the Cu–Ce–O system, however, we do not regard the copper cluster as distinct fine metallic copper or Cu_2O particles but rather as a group of copper atoms. We postulate that the presence of copper ions in the Cu–Ce(La)–O systems may increase the concentration of unsaturated cerium ion (Ce^{3+}) and the concentration of the superoxide species.

Most of the experimental observations in this work can be explained with this reaction model. First of all, based on the model, only a small amount of copper or gold is needed to form an active catalyst. Bulk CuO oxide does not contribute to the observed CO oxidation activity. Isolated copper ions, as found in the $Cu_{0.01}[Ce(La)]_{0.9}O_x$ catalyst prepared by calcination under nitrogen, are not active because they can be capped by oxygen and water molecules so that the CO adsorption sites are greatly suppressed. In the Cu–Zr–O system, copper clusters may be stabilized by zirconia through the interstitial interaction model in Fig. 18, but the high stability of Zr^{4+} ions would not favor the formation of superoxide species (O_2^-) and the Cu^+ species. This may be the reason why the Cu–Zr–O catalyst showed greatly improved resistance to water vapor poisoning but only a small enhancement in catalytic activity compared to bulk CuO catalyst as reported in the preceding paper (1).

4.4. Methane Oxidation Kinetics

A variety of kinetic models for methane combustion on metal oxides have been reported (39, 40). The activation energy for methane oxidation over the $Cu_{0.15}[Ce(La)]_{0.85}O_x$ catalyst is comparable to that reported in the literature data. In general, the rates on base metal oxides such as perovskite-type mixed oxides are first-order in methane, while the order in oxygen may vary from zero to approximately 0.5. A noncompetitive Langmuir–Hinshelwood kinetic model was proposed by Otsuka *et al.* (41) for oxidative coupling of methane over a Ba-doped CeO_2 catalyst. However, all previous kinetic studies used a narrower window of partial pressure of methane (P_m) than the present work. The Langmuir-adsorption-type dependence on P_m in the kinetic expression (Eq. [7]) for methane oxidation over the $Cu_{0.15}[Ce(La)]_{0.85}O_x$ catalyst suggests that the rate-determining step involves adsorbed methane. The power order dependence on the partial pressure of oxygen (P_O) suggests complex oxygen sources for the reaction. The following reaction mechanism is proposed based on the present kinetic results:

$$CH_{4,cat} + O^-_{cat} \xrightarrow{\text{slow}} CH^-_{3,cat} + HO_{cat} \quad [13]$$

$$CH^-_{3,cat} + O_{cat} \xrightarrow{\text{fast}} O^-_{cat} + CH^{\cdot}_{3,cat} \xrightarrow{\text{oxidation}} CO_2 + H_2O. \quad [14]$$

In the above equations, "cat" denotes catalyst surface. Gas phase oxygen can quickly reach equilibrium with the various surface oxygen species as described by Eq. [12]. The rate-limiting step involves the reaction of adsorbed methane with the surface basic groups (oxygen ions). The negative charge on the resulting methyl group can transfer to the surface oxygen through the electronic band or a metal ion intermediate (e.g., $M^{n+} + e^- \rightarrow M^{(n-1)+} + O_{cat} \rightarrow M^{n+} + O^-_{cat}$). The methyl radical is rapidly and completely oxidized into carbon dioxide and water over the present catalyst. This mechanism is, overall, similar to the ones proposed in the literature for methane oxidation over base metal oxide catalysts. But, some previous kinetic studies of methane combustion suggest the direct reaction of gaseous methane with the catalyst surface. Given the low-temperature activity of the catalysts reported here, it is plausible to suggest methane adsorption on the catalyst surface as a necessary activation step.

Although it has a similar rate expression to CO oxidation, the methane oxidation process may be intrinsically different from CO oxidation. The preexponential factor of the methane oxidation rate constant in Eq. [8] is about five orders of magnitude smaller than that of the CO oxidation rate constant in Table 2. The heat of methane adsorption on the $Cu_{0.15}[Ce(La)]_{0.85}O_x$ catalyst is only about 14.2 kJ/mol. The Cu^+ species provide sites for strong CO adsorption but not for that of methane. Van Kooten *et al.* (42) found no measurable interaction of methane with metallic and oxidized copper over the temperature range of 300 to 750 K. At the present time, we do not know

the specific surface sites for methane adsorption on the Cu–Ce(La)–O catalyst. Regarding the oxygen source, Li *et al.* (43) observed that methane oxidation on cerium oxide occurred in the absence of gaseous oxygen and superoxide species, which were considered to be active for CO oxidation. Our fixed-bed, steady-state measurements of CO and methane oxidation found that the two reactions were virtually independent of each other. Methane oxidation over the Cu–Ce(La)–O catalyst occurred at higher temperatures (>300°C). Although such temperatures may not be high enough to cause significant bulk oxygen mobility, the participation of surface capping (O_2^{2-}, O^-, or O^{2-}) and lattice oxygen is very likely since surface species on the CeO_2 surface are more active than the bulk (33, 44). In conclusion, methane oxidation is a more complicated process than CO oxidation and a detailed adsorption/desorption study is necessary to elucidate the reaction mechanism.

5. SUMMARY

Gold in the $Au_{0.05}[Ce(La)]_{0.95}O_x$ catalyst exists in fine metallic particles in contact with the cerium oxide. The CO oxidation kinetics over the $Au_{0.05}[Ce(La)]_{0.95}O_x$ catalyst were described by a rate equation such as $kP_{CO}^{0.30}P_O^{0.18}$.

Copper in small amounts showed strong tendency to attach to cerium oxide surface irrespective of catalyst preparation. Copper in the Cu–Ce–O composite existed in the form of isolated ions, clusters, and bulk CuO particles. Isolated ions aggregated into clusters after heating at high temperatures (≥650°C) in air. When the cerium oxide surface was saturated by copper clusters, excess copper formed bulk CuO particles which were typically covered by the fine cerium oxide particles. Cu^{+1} species was observed with all the Cu–Ce–O catalysts in the XPS studies and its formation is considered to originate from the interaction of copper clusters with cerium oxide.

The oxidation rates of CO and methane over the Cu–Ce(La)–O catalysts were expressed as $kK_RP_R/P_O^n/(1 + K_RP_R)$, where P_R denotes the partial pressure of CO or methane and P_O is the partial pressure of oxygen. The activation energies of the surface reactions were 78–94 kJ/mol for CO oxidation and 79 kJ/mol for methane oxidation, respectively. The heat of adsorption on the Cu–Ce–O catalyst was in the range of 28 to 62 kJ/mol for CO adsorption and 14 kJ/mol for methane adsorption, respectively.

The Langmuir–Hinshelwood mechanism and a synergistic reaction model were proposed for CO oxidation over the Cu–Ce–O and Au–Ce–O catalysts. In this model, the Cu^+ species of a copper cluster or fine gold particles provide sites for CO adsorption, cerium oxide provides the oxygen source, and the reaction proceeds at the boundary of the two kinds of materials. The Langmuir–Hinshelwood mechanism was also proposed for methane oxidation over the Cu–Ce–O catalyst.

APPENDIX: NOTATION

E_a	Activation energy (kJ/mol)
E_{app}	Apparent activation energy (kJ/mol)
k	Reaction constant (mol/(g · s · bar^{m+n}))
k_{CO}	Reaction constant of CO oxidation (mol/(g · s · bar^n))
k_m	Reaction constant of methane oxidation (mol/(g · s · bar^n))
K_{CO}	CO adsorption equilibrium constant (1/bar)
K_m	Methane adsorption equilibrium constant (1/bar)
K_O	Adsorption equilibrium constant of reacting species (1/bar)
m, n	Reaction orders
N_t	Total gas flow rate (mol/s)
P	Total pressure of reacting gases mixture (bar)
P_{CO}	Partial pressure of CO (bar)
P_{CO_2}	Partial pressure of CO_2 (bar)
P_m	Partial pressure of methane (bar)
P_O	Partial pressure of oxygen (bar)
P_R	Partial pressure of reacting species (bar)
Q	Heat of adsorption (kJ/mol)
R	Gas constant (J/mol · K)
R_{CO}	Reaction rate of CO oxidation (mol · s)
R_m	Reaction rate of methane oxidation (mol/g · s)
T	Reaction temperature (K)
W_{cat}	Weight of catalyst loading (g)
X_{CO_2}	Conversion to CO_2

ACKNOWLEDGMENTS

This work has been supported by the U.S. Department of Energy, University Coal Research Program, under Grant DE-FG22-92PC92534. The authors thank Dr. A. Garratt-Reed for the STEM analyses and reviewers of this manuscript for their comments and suggestions. This work made use of the MRSEC Shared Facilities supported by the National Science Foundation under Award DMR-9400334.

REFERENCES

1. Liu, W., and Flytzani-Stephanopoulos, M., *J. Catal.* **153,** (1995).
2. Tauster, S. J., Fung, S. C., Baker, R. T. K., and Horsley, J. A., *Science* **211,** 1121 (1981).
3. Baker, R. T. K., Tauster, S. J., and Dumesic, J. A. (Eds.), "Strong Support Interactions." Am. Chem. Soc., Washington, DC, 1986.
4. Stevenson, S. A., Dumesic, J. A., Baker, R. T. K., and Ruckenstein, E., (Eds.), "Metal–Support Interactions in Catalysis, Sintering, and Redispersion." Van Nostrand–Reinhold, New York, 1987.
5. Narayan, S., *J. Sci. Ind. Res.* **44,** 580 (1985).
6. Burch, B., and Flambard, A. R., *J. Catal.* **78,** 389 (1982).
7. Bell, A. T., *in* "Catalyst Design, Process and Perspectives," (L. L. Hegedus, *et al.*, Eds.), p. 103. Wiley, New York, 1987.
8. Frost, J. C., *Nature* **334,** 577 (1988).

9. Crucq, A., (Ed.), "Catalysis and Automotive Pollution Control II." Elsevier, Amsterdam, 1991.
10. Metcalfe, I. S., and Sundaresan, S., *AICHE J.* **34,** 195 (1988).
11. Schryer, D. R., Upchurch, B. T., Sidney, B. D., Hoflund, G. B., and Herz, R. K., *J. Catal.* **130,** 314 (1991).
12. Boulahouache, A., Kous, G., Lintz, H.-G., and Schulz, P., *Appl. Catal. A: General* **9,** 115 (1990).
13. Sheintuch, M., Schmidt, J., Lecthman, Y., and Yahav, G., *Appl. Catal.* **49,** 55 (1989).
14. Haruta, M., Tsubota, S., Kobayashi, T., Kageyma, H., Genet, M. J., and Delmon, B., *J. Catal.* **144,** 175 (1993).
15. Dow, W. P., and Huang, T. J., *J. Catal.* **147,** 322 (1994).
16. Wagner, C. D., Riggs, W. M., Davis, L. E., Moulder, J. F., and Muilenberg, G. E., (Eds.), "Handbook of X-ray Photoelectron Spectroscopy." Perkin—Elmer Corp., Palo Alto, CA, 1978.
17. Agudo, A. L., Palacios, J. M., Fierro, J. L. G., Laine, J., and Severio, F., *Appl. Catal. A: General* **91,** 43 (1992).
18. Jernigan, G. G., and Somorjai, G. A., *J. Catal.* **147,** 567 (1994).
19. Siriwardane, R. V., and Poston, J. A., *Appl. Surf. Sci.* **68,** 65 (1993).
20. Shpiro, E. S., Grunert, W., Joyner, R. W., and Baeva, G. N., *Catal. Lett.* **24,** 159 (1994).
21. Jin, T., Zhou, Y., Mains, G. J., and White, H. M., *J. Phys. Chem.* **91,** 5931 (1987).
22. Arai, T., Maruya, K., Domen, K., and Onishi, T., *J. Catal.* **141,** 533 (1993).
23. Abou kais, A., Bennani, A., Aissi, C. F., Guelton, M., and Vedrine, J., *Chem. Mater.* **4,** 977 (1992).
24. Abou kais, A., Bennani, A., Aissi, C. F., Wrobel, G., and Guelton, M., *J. Chem. Soc. Faraday Trans.* **89**(9), 1321 (1992).
25. Soria, J., Conesa, J. C., Martinez-Arias, A., and Coronado, J. M., Bechara, *Solid State Ionics* **63–65,** 755 (1993).
26. Dekker, N. J. J., Hoorn, J. A. A., Stegenga, S., Kapteijn, F., and Moulijn, J. A., *AICHE J.* **38,** 385 (1992).
27. Choi, K. I., and Vannice, M. A., *J. Catal.* **131,** 22 (1991).
28. Klimisch, R. L., and Taylor, K. C., *Science* **179,** 798 (1973).
29. Clarke, D. B., Suzuki, I., and Bell, A. T., *J. Catal.* **142,** 27 (1993).
30. Sandval, M. J., and Bell, A. T., *J. Catal.* **144,** 227 (1993).
31. Sze, S. M., "Physics of Semiconductor Devices," 2nd ed. Wiley, New York, 1981.
32. Yao, H. C., and Yao, Y. F. Y., *J. Catal.* **86,** 254 (1984).
33. Li, C., Domen, K., Maruya, K. I., and Onishi, T., *J. Am. Chem. Soc.* **111,** 7683 (1989).
34. Li, C., Domen, K., Maruya, K. I., and Onishi, T., *J. Catal.* **123,** 436 (1990).
35. Zhang, X., and Klabunde, K. J., *Inorg. Chem.* **31,** 1706 (1992).
36. Li, C., Chen, Y., Li, W., and Xin, Q., "New Aspects of Spillover in Catalysis, (T. Inui, *et al.*, Eds.), p. 217. Elsevier, Amsterdam, 1993.
37. Martin, D., and Duprez, D., in Inui, T., *et al.* (Eds.), "New Aspects of Spillover in Catalysis," (T. Inui, *et al.*, Eds.), p. 201, Elsevier, Amsterdam, 1993.
38. Tarasov, A. L., Przheval'skaya, L. K., Shvets, V. A., and Kazanskii, V. B., *Kinet. Katal.* **29,** 1181 (1988).
39. Seiyama, T., *Catal. Rev.-Sci. Eng.* **34,** 281 (1992).
40. Zwinkels, M. F. M., Jaras, S. G., and Menon, P. G., *Catal. Rev.-Sci. Eng.* **35,** 319 (1993).
41. Otsuka, K., Komatsu, T., and Shimizu, Y., *in* "Successful Design of Catalysts," (T. Inui, Ed.), p. 43. Elsevier, Amsterdam, 1988.
42. van Kooten, W. E. J., Kragten, D. D., Gijzeman, O. L. J., and Geus, J. W., *Surf. Sci.* **290,** 302 (1993).
43. Li, C., Xin, Q., Guo, X., and Onishi, T., *in* New Frontiers in Catalysis, Proceedings, 10th International Conference on Catalysis, July 19–24, Budapest, Hungary, 1992" (L. Guczi, *et al.*, Eds.), p. 1955. Elsevier, Amsterdam 1993.
44. Sayle, T. X. T., Parker, S. C., and Catlow, C. R. A., *J. Chem. Soc. Chem. Commun.*, 977 (1992).